

# Inferring symbolic dynamics of chaotic flows from persistence

Gökhan Yalnız<sup>1</sup> and Nazmi Burak Budanur<sup>2</sup>

<sup>1</sup>*Physics Department, Boğaziçi University, 34342 Istanbul, Turkey*

<sup>2</sup>*Nonlinear Dynamics and Turbulence Group, IST Austria, 3400 Klosterneuburg, Austria<sup>a)</sup>*

(Dated: 11 October 2024)

We introduce state space persistence analysis for deducing the symbolic dynamics of time-series data obtained from high-dimensional chaotic attractors. To this end, we adapt a topological data analysis technique known as persistent homology for the characterization of state space projections of chaotic trajectories and periodic orbits. By comparing the shapes along a chaotic trajectory to those of the periodic orbits, state space persistence analysis quantifies the geometric similarities of chaotic trajectory segments and the periodic orbits. We demonstrate the method by applying it to the three-dimensional Rössler system and a thirty-dimensional discretization of the Kuramoto-Sivashinsky partial differential equation in  $(1 + 1)$  dimensions.

Keywords: high-dimensional chaos, symbolic dynamics, topological data analysis, persistent homology

**One way of studying chaotic attractors systematically is through their symbolic dynamics, in which one partitions the state space into qualitatively different regions and assigns a symbol to each such region. This yields a coarse-grained state space of the system which can then be reduced to a Markov chain encoding all possible transitions between the states of the system. While it is possible to obtain the symbolic dynamics of low-dimensional chaotic systems with standard tools such as Poincaré maps, when applied to high-dimensional systems such as turbulent flows, these tools alone are not sufficient to determine their symbolic dynamics. In this paper, we develop the state space persistence analysis and demonstrate that it can be utilized to infer the symbolic dynamics in very high-dimensional settings.**

## I. INTRODUCTION

One of the defining features of chaos is the sensitive dependence on initial conditions,<sup>1</sup> which is a statement of the exponential amplification of noise under chaotic dynamics. The practical corollary of this fundamental property is that any prediction based on integrating equations of motion of a chaotic system starting from an initial condition is exponentially wrong in time since all measurements come with noise. Thus, even with the advanced computing technologies of our day, the question of “What is the future state of a chaotic system based on a measurement of its current state?” can only be answered for a finite-time horizon. A different and more tractable question is the following: What are the possible future states of a chaotic system given an approximate measurement

of its current state? The answer to this question begins with the classification of the system’s set of states with qualitative differences and the associated methods of the dynamical systems theory are known as symbolic dynamics.<sup>1,2</sup> While these techniques lie at the heart of some of the most fundamental results of chaos theory such as the Smale horseshoe,<sup>3</sup> existing symbolic dynamics methods can only be applied to low-dimensional systems, namely the ones that can be effectively described by one- or two-dimensional maps.

Many real-life situations, in which chaos prevails against orderly motion, take place in systems with many ( $D \gg 3$ ) degrees of freedom. Examples include fluid turbulence,<sup>4</sup> cardiac dynamics,<sup>5</sup> and evolution.<sup>6</sup> Generally, such systems cannot be reduced to low-dimensional maps, except in special cases close to the onset of chaos.<sup>7</sup> However, the observations based on computer simulations<sup>8–10</sup> suggest that high-dimensional systems such as turbulent flows exhibit a large catalog of motions that can be associated with the time-periodic solutions of the governing equations. While the methods for locating unstable periodic orbits of high-dimensional dynamical systems are well-developed,<sup>11</sup> to the best of our knowledge, there exists no technique for the unsupervised identification of similarities between chaotic trajectory segments and periodic orbits of high-dimensional systems. In this paper, we shall demonstrate that this can be achieved via topological data analysis.

In this paper, we propose a novel technique for inferring the symbolic dynamics of chaotic motion in arbitrary dimensions. We name our method “state space persistence analysis”, and illustrate its core ideas on the three-dimensional Rössler system. We then apply the method to the Kuramoto-Sivashinsky partial differential equation (PDE) and show that the system’s spatiotemporally chaotic dynamics can be approximated by a Markov chain based on four distinct periodic orbits. The rest of the paper is organized as follows. In section II, we recapitulate the core concepts from the dynamical systems theory and topological data analysis, which form the foundations of state space persistence analysis. In

<sup>a)</sup>Electronic mail: [burak.budanur@ist.ac.at](mailto:burak.budanur@ist.ac.at)

section III, we lay out the steps of state space persistence analysis for a generic dynamical system. We demonstrate our method with applications in section IV, discuss our results in section V and conclude in section VI.

## II. PRELIMINARIES

We consider dynamical systems defined by a  $D$ -dimensional state space  $\mathcal{M} \subset \mathbb{R}^D$  and a smooth flow map  $f^t(\xi)$  that maps state vectors  $\xi \in \mathcal{M}$  as

$$\xi(t) = f^t(\xi(0)), \quad (1)$$

where  $t \in \mathbb{R}^+$  is the time variable. Although it is not a general requirement, in the examples we are going to consider,  $f^t(\xi(0))$  will be related to an ordinary differential equation (ODE)

$$\dot{\xi} = v(\xi) \quad (2)$$

through the relation

$$f^t(\xi(0)) = \xi(0) + \int_0^t v(\xi(t')) dt', \quad (3)$$

where  $v(\xi)$  is called the state space velocity. While in the examples worked out here we always use the Euclidean or  $L_2$  inner product

$$\langle \xi^{(i)}, \xi^{(j)} \rangle = \sum_{k=1}^D \xi_k^{(i)} \xi_k^{(j)}, \quad (4)$$

we expect that the topological methods we develop here do not depend strongly on the particular choice of norm.

### II.1. Symbolic dynamics and shadowing

We assume that the state space  $\mathcal{M}$  is coarse-grained into sub-regions  $\mathcal{M}_A, \mathcal{M}_B, \mathcal{M}_C \dots$  such that a trajectory  $\xi(t)$  for  $t \in (0, t_F)$  can be associated with an itinerary  $\sigma_1 \sigma_2 \sigma_3 \dots$  with  $\sigma_i \in \{A, B, C, \dots\}$  according to the successive state space regions visited by the trajectory. Further, we assume that the system admits periodic orbits such that every point  $\xi_p$  on a periodic orbit  $p$  satisfies

$$\xi_p = f^{T_p}(\xi_p), \quad (5)$$

for a nonzero period  $T_p$  and its integer multiples. By definition, a periodic orbit has a cyclic itinerary, such as  $\overline{\sigma_1 \sigma_2 \dots \sigma_n}$ , where the overline denotes infinite repetition. In what follows we are going to use the itinerary of a periodic orbit as its label, when an itinerary is known. Finally, we assume that the first  $n$  symbols in the itinerary of a trajectory  $\xi(t)$  for  $t \in (0, t_F)$  will be same with that of the periodic point  $\xi_p$  if  $\xi(0)$  and  $\xi_p$  are sufficiently close in an appropriately defined state space distance measure. When a segment of an itinerary of a generic trajectory is

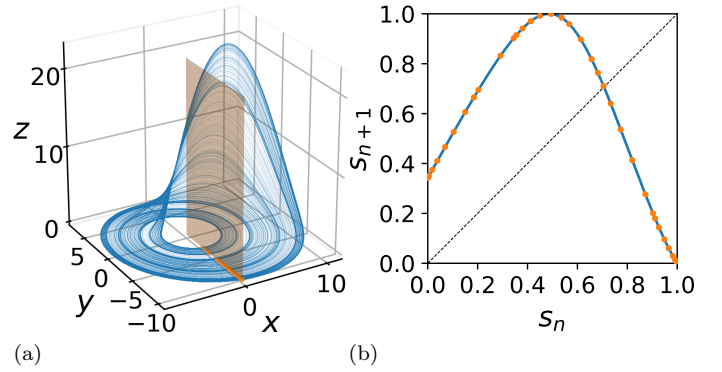


FIG. 1. (a) A trajectory (blue) on the Rössler attractor, with part of its intersections (orange points) with the Poincaré section (7), which is visualized as a transparent surface. (b) Poincaré map parameterized with the arc length on the curve along the intersections, with its interpolation (blue curve) and part of the intersections (orange). In both cases, only every tenth intersection is shown for visibility.

the same with that of a periodic orbit, we say that “the trajectory shadows the periodic orbit”. Let us illustrate these concepts with an example.

The Rössler system is defined by the set of ODEs

$$\dot{x} = -(y+z), \quad \dot{y} = x+0.2y, \quad \dot{z} = 0.2+z(x-5.7). \quad (6)$$

The numerical integration of (6) yields a chaotic attractor visualized as a long trajectory in Fig. 1 (a). We define a Poincaré section  $\hat{\mathcal{M}}$  as the half-hyperplane of points  $\hat{\xi} \in \hat{\mathcal{M}}$ , which satisfy

$$\langle \hat{\xi} - \hat{\xi}', \eta \rangle = 0 \quad \text{and} \quad \langle v(\hat{\xi}), \eta \rangle > 0, \quad (7)$$

where  $\hat{\xi}'$  and  $\eta$  are called the “section template” and the “section normal”, respectively. For the choices of  $\hat{\xi}' = (0, -1, 0)$  and  $\eta = (1, 0, 0)$  we visualized the Poincaré section defined by (7) in Fig. 1 (a) as a transparent surface.

Let  $\hat{\xi}[n]$  be a state vector on the Poincaré section (7) at the discrete-time  $n$ . The Poincaré map is the discrete time system

$$\hat{\xi}[n+1] = \mathcal{P}(\hat{\xi}[n]) = f^{\Delta t_n}(\hat{\xi}), \quad (8)$$

where  $\Delta t_n$  is the “first return time”, that is, the minimum time required for the trajectory of  $\hat{\xi}[n]$  to intersect the Poincaré section (7). As illustrated by Fig. 1 (a), the trajectories on the Rössler attractor intersect the Poincaré section (7) along what appears to be a one-dimensional curve. This suggests the arclength along this curve as a natural parametrization for the Poincaré map. We interpolate this curve with cubic splines and use the data to obtain the unimodal Poincaré return map shown in Fig. 1 (b).

We are now in position to partition the state space of Rössler system into subregions. The return map of

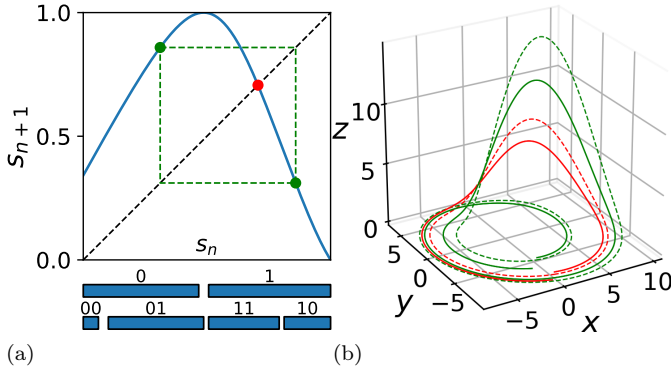


FIG. 2. (a) Periodic orbits  $\bar{1}$  (red point),  $\bar{01}$  (green points, connected with dashed line segments) and the partitioning of the Rössler system’s Poincaré map. (b) Periodic orbits  $\bar{1}$  (red, dashed),  $\bar{01}$  (green, dashed) and shadowing trajectory segments (same colors, solid) of the Rössler system.

Fig. 1 (b) has one critical point  $\hat{\xi}_c = 0.4868$ , at which the derivative of the Poincaré map is zero. Let us define subregions  $\hat{\mathcal{M}}_0$  and  $\hat{\mathcal{M}}_1$  as

$$\hat{\mathcal{M}}_0 = \{\hat{\xi} \in \hat{\mathcal{M}} \mid \hat{\xi} < \hat{\xi}_c\}, \quad (9)$$

$$\hat{\mathcal{M}}_1 = \{\hat{\xi} \in \hat{\mathcal{M}} \mid \hat{\xi} > \hat{\xi}_c\}. \quad (10)$$

With these definitions, we can now assign each trajectory on the Rössler attractor a binary symbol sequence. In particular, we can now enumerate the periodic orbits of the Rössler system with binary numbers. Fig. 2 (a) shows the two shortest periodic orbits  $\bar{1}$  and  $\bar{01}$  of the Rössler system on the Poincaré map and Fig. 2 (b) shows these orbits in the full state space.

It is straightforward to confirm that a point on the Poincaré map Fig. 2 (a) that is close to a periodic orbit will initially have the same itinerary as that of the periodic orbit. We show examples of such “shadowing” trajectories along with the periodic ones in Fig. 2 (b). At the bottom of Fig. 2 (a), we show the second order partitioning of the unimodal map with respect to the itineraries of the points on it. This partitioning can be confirmed by inspection. In fact, further iterates of the map would result in finer partitions with longer and longer periodic orbits. For details, we refer the interested reader to Refs. 1 and 2.

The similarities of the periodic orbits and the shadowing trajectory segments in Fig. 2 (b) constitute the key intuition of state space persistence analysis. In general, it is not possible to reduce the dynamics of a chaotic attractor into a unimodal map such as Fig. 1 (b). However, one can still find periodic orbits and compare the shapes of trajectory segments to those of the periodic orbits. Our next step is to introduce persistent homology which we will utilize for this purpose.

## II.2. Persistent homology

Persistent homology is a mathematical framework for extracting significant topological features of a data set. In this section, we illustrate the persistent homology concepts that we are going to incorporate in our method through an example, while trying to avoid the technical language as much as possible. For in-depth introductions, we refer the reader to the survey<sup>12</sup> and the textbook<sup>13</sup> by Edelsbrunner and Harer and the “roadmap”<sup>14</sup> by Otter *et al.*

In our applications, we are going to consider a data set

$$\Xi = \{\tilde{\xi}^{(1)}, \tilde{\xi}^{(2)}, \dots, \tilde{\xi}^{(N)}\} \quad (11)$$

that is composed of projections  $\tilde{\xi}^{(i)} = \mathbf{P}\xi^{(i)}$  of state vectors sampled from a trajectory of a dynamical system, where the rows of  $\mathbf{P}$  are going to be some projection bases specific to our application. Fig. 3 (a) shows an example of such a data set from the Rössler system as a projection onto the  $(x, y)$ -plane. These points were sampled from the periodic orbit  $\bar{1}$  (Fig. 2) of the Rössler system with a constant time step.

For the analysis to follow, we need a distance function for the projected data set, which we define as

$$d(\tilde{\xi}^{(i)}, \tilde{\xi}^{(j)}) = \left\langle \tilde{\xi}^{(i)} - \tilde{\xi}^{(j)}, \tilde{\xi}^{(i)} - \tilde{\xi}^{(j)} \right\rangle^{1/2}. \quad (12)$$

Let  $d_r \geq 0$  be the “resolution” (a distance parameter),  $\Xi_{d_r}$  denote a continuous sequence of sets of subsets of  $\Xi$  parameterized by  $d_r$ , and  $\Xi_0 = \{\{\tilde{\xi}^{(1)}\}, \{\tilde{\xi}^{(2)}\}, \dots, \{\tilde{\xi}^{(N)}\}\}$ .  $\Xi_{d_r}$  is formed by the union of  $\Xi_0$  with all edges  $\{\tilde{\xi}^{(i)}, \tilde{\xi}^{(j)}\}$ , such that  $d(\tilde{\xi}^{(i)}, \tilde{\xi}^{(j)}) \leq d_r$ , and all triangles  $\{\tilde{\xi}^{(i)}, \tilde{\xi}^{(j)}, \tilde{\xi}^{(k)}\}$  such that all pairwise distances  $d(\tilde{\xi}^{(i,j,k)}, \tilde{\xi}^{(i,j,k)}) \leq d_r$ . We visualized  $\Xi_{d_r}$  for different values of  $d_r$  in Fig. 3 (a-f).

As we vary  $d_r$  from 0 to  $\infty$ , we are going to keep track of the number of components and holes in  $\Xi_{d_r}$ . By a “component”, we refer to an individual point or a set of points and the edges that connect them and all triangles that fill the space in between. A “hole” is formed when a component is in the form of a loop with not-necessarily-distinct inner and outer boundaries.

For example, in Fig. 3 (a), we have 14 components, whereas in Fig. 3 (b), we have 6. In Fig. 3 (c), the single component of  $\Xi_{d_r=5.07}$  forms a loop with a hole. As we further increase  $d_r$ , triangles begin to form (Fig. 3 (d-e)), and finally the hole is completely filled with triangles at  $d_r = 13.3$  (Fig. 3 (f)). This sequence of appearances and disappearances of shapes can be encoded into diagrams such as the ones in Fig. 4. Fig. 4 (a) is called a barcode diagram, where components (red) and holes (blue) are represented by bars that span the interval of  $d_r$  for which the respective object can be observed. Another graphical representation of the same information is the so-called “persistence diagram”, on which the birth and death coordinates  $(d_{r,B}, d_{r,D})$  of components and holes are marked as shown in Fig. 4. We would like to note here

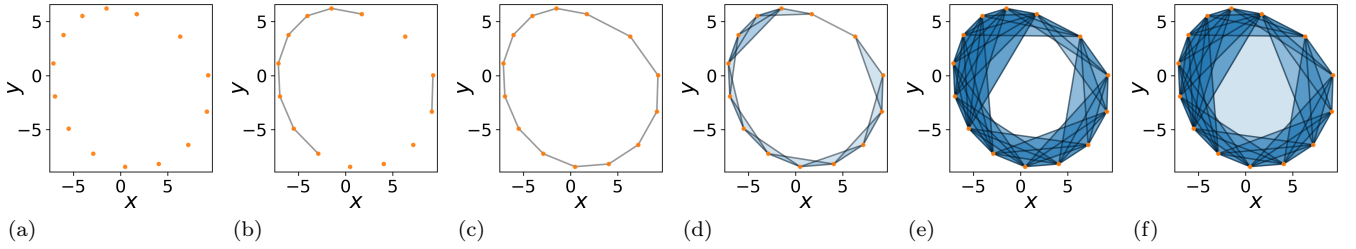


FIG. 3. Sequence of sets  $\Xi_{d_r}$  corresponding to a data set sampled from the periodic orbit  $\bar{1}$  of the Rössler system. In all figures, the initial data points are shown orange, edges connecting them are drawn as line-segments, and triangles are visualized as transparent blue fillings. (a)  $d_r = 0$ , (b)  $d_r = 3.5$ , (c)  $d_r = 5.07$ , (d)  $d_r = 8.0$ , (e)  $d_r = 13.2$ , (f)  $d_r = 13.3$ .

that when two points are connected by an edge, which of the two points has died is ambiguous. This ambiguity, however, does not have an effect on the barcode and persistence diagrams since both points appear at  $d_r = 0$ .

Given a data set  $\Xi$ , the object that is of interest to us will be the associated persistence diagram  $\text{PD}(\Xi)$ . In general, the elements that are further away from the diagonal of a persistence diagram are said to be the more significant features of the data set, since they live longer. Persistence diagrams are stable in the sense that if the samples in the data set  $\Xi$  are slightly perturbed, then the associated persistence diagram also changes only slightly. We illustrate this in Fig. 4 (c) where we show the persistence diagram associated with a data set sampled from a Rössler trajectory that shadows the periodic orbit  $\bar{1}$  in Fig. 2 (b) next to the persistence diagram of the  $\bar{1}$ . A proof of the stability of persistence diagrams can be found in Ref. 15.

We quantify the similarity of two persistence diagrams by defining a distance between diagrams. Let us first define the set of diagonal elements  $\Delta = \{(d_{r,B}, d_{r,D}) \in [0, \infty) \times [0, \infty) \mid d_{r,B} = d_{r,D}\}$ .  $\Delta$  corresponds to the trivial persistence diagram elements that are born and dead at the same  $d_r$  value. We can also denote the components and holes on a persistence diagram by the sets

$$\text{PD}_i = \{(d_{r,B}, d_{r,D})_1, (d_{r,B}, d_{r,D})_2, \dots, (d_{r,B}, d_{r,D})_N\} \cup \Delta \cup \Delta \cup \Delta \dots, \quad i \in \{0, 1\}, \quad (13)$$

where  $i = 0$  corresponds to the components and  $i = 1$  corresponds to the holes in a diagram. We included the trivial sets with infinite multiplicity into the persistence diagrams for a reason which will be apparent soon. We are now in position to define a distance metric between the persistence diagrams  $\text{PD}^{(n)}$  and  $\text{PD}^{(m)}$ . Let  $\phi : \text{PD}_i^{(n)} \rightarrow \text{PD}_i^{(m)}$  be a bijection that pairs each element of  $\text{PD}_i^{(n)}$  with exactly one element of  $\text{PD}_i^{(m)}$ . We define the  $p^{\text{th}}$  Wasserstein distance between  $\text{PD}_i^{(n)}$  and

$\text{PD}_i^{(m)}$  as

$$W_p(\text{PD}_i^{(n)}, \text{PD}_i^{(m)}) = \inf_{\phi} \left[ \sum_{\mu \in \text{PD}_i^{(n)}} \|\mu - \phi(\mu)\|_q^p \right]^{1/p}, \quad (14)$$

where  $p \in [1, \infty]$ ,  $q \in [1, \infty]$ , and  $\|\cdot\|_q$  denotes the  $L_q$ -norm in  $\mathbb{R}^2$ . When  $p = 1$ , the Wasserstein distance (14) can be understood as the smallest possible sum of the lengths of the line segments that can be drawn from the elements of  $\text{PD}_i^{(n)}$  to those of  $\text{PD}_i^{(m)}$ . The addition of diagonal elements to the persistence diagrams makes it possible to compare very different diagrams with possibly different number of nontrivial elements by allowing matching the nontrivial elements of one diagram to the diagonal of the other. Setting  $p > 1$  emphasizes the contributions from the elements that are further away from the diagonal in comparison to others, i.e. the ones that are more persistent against the changes in  $d_r$ .

This concludes our overview of the persistent homology concepts that we are going to incorporate into state space persistence analysis. There are various algorithms and implementations for computing persistence diagrams and their Wasserstein distances (14), which are not in the scope of the current work. For a review, we refer the interested reader to Ref. 14. In the applications that we are going to present in section IV, we utilized the programs `Ripser`<sup>16</sup> for the computation of persistence diagrams and `Hera`<sup>17,18</sup> for the computation of the Wasserstein distance.

### III. STATE SPACE PERSISTENCE ANALYSIS

In this section, we are going to list the basic steps of state space persistence analysis for capturing the symbolic dynamics of high-dimensional chaotic flows. Although we believe that the method is general and can be used in any flow, primary applications we have in mind are discretizations of nonlinear PDEs such as the Navier-Stokes equations. In the following, we list the steps of state space persistence analysis for a typical nonlinear PDE.

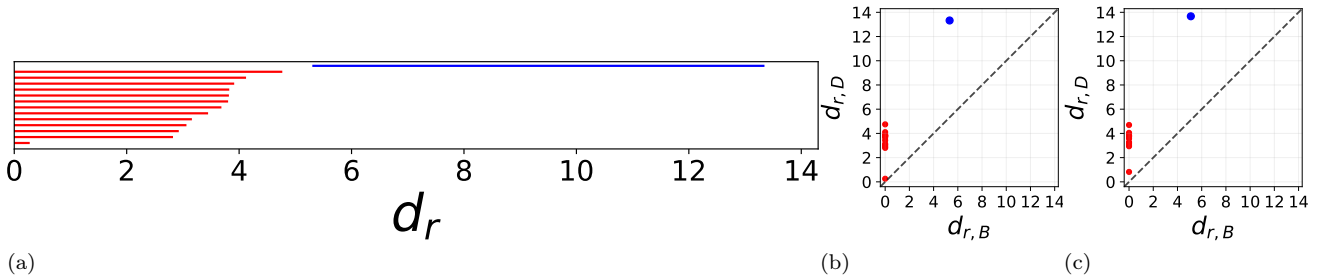


FIG. 4. (a) Barcode diagram showing the birth and death of components (red) and holes (blue) as  $d_r$  increases corresponding to the data set shown in Fig. 3. (b) Persistence diagram on which the "Birth" and "Death" coordinates  $(d_{r,B}, d_{r,D})$  of the components and holes are marked red and blue respectively. (c) Persistence diagram obtained from a Rössler system trajectory which shadows the periodic orbit  $\bar{I}$  as shown in Fig. 2 (b).

### III.1. Symmetry reduction

Nonlinear PDEs are usually equivariant under a certain set of symmetries such as translations, rotations, and reflections. These symmetries tend to obscure the dynamics by increasing the data volume since each solution has a set of symmetry copies that are also solutions. Furthermore, systems with continuous symmetries tend to have higher dimensional invariant solutions such as relative periodic orbits,<sup>2,19</sup> which are periodic orbits up to continuous symmetry transformations.

For the state space persistence analysis, we are going to assume that  $(\mathcal{M}, f^t)$  is a symmetry-reduced realization of the dynamical system under consideration. In other words, before we begin our analysis, we carry out a symmetry-reducing coordinate transformation, which maps each symmetry-equivalent solution of the system to a single representative  $\xi \in \mathcal{M}$ . This, in general, can be a nontrivial task. However, there has been considerable development in recent years following the introduction of "first Fourier mode slice" by Budanur *et al.*<sup>20</sup> It is a straightforward method for reducing the  $SO(2)$ -symmetry due to translation-equivariance and periodic boundary conditions. Since then, this method was adapted to the two-dimensional Kolmogorov flow,<sup>21</sup> three-dimensional pipe flow,<sup>22,23</sup> one-dimensional Korteweg-de Vries equation,<sup>24</sup> and pilot-wave hydrodynamics.<sup>25</sup> For a pedagogical introduction to the first Fourier mode slice, we refer the reader to Ref. 26. The reduction of discrete-symmetries can also be nontrivial. The only discrete symmetry-reduction method for high-dimensional systems in the literature known to us is the invariant polynomials for reflection-type symmetries.<sup>27</sup> We are going to present the symmetry reduction of the Kuramoto-Sivashinsky system in appendix A.

### III.2. Base set of periodic orbits

We are going to search for a base set of periodic orbits  $\bar{p}\bar{o} = \{\bar{p}\bar{o}_1, \bar{p}\bar{o}_2, \dots, \bar{p}\bar{o}_M\}$ , with which we are going to attempt to approximate chaotic dynamics. In gen-

eral, this step will be experimental and could be reiterated following a performance analysis. Generically, this set of periodic orbits can be found via recurrence-based searches<sup>8-11,28</sup> or following bifurcations<sup>7,29</sup> and unstable manifolds of known solutions.<sup>27,30</sup> While there exists variational,<sup>30</sup> Levenberg-Marquadt search-based,<sup>28</sup> and possibly various other optimization methods for numerically locating unstable periodic orbits, current community standard for very-high-dimensional flows is the Newton-Krylov-hookstep method of Viswanath.<sup>11</sup>

### III.3. Local persistence of periodic orbits

We are going to sample the states  $\xi^{(\bar{p}\bar{o}_i)}(t)$  on each periodic orbit  $\bar{p}\bar{o}_i$  with a constant sampling time  $t_s$  and construct local projection bases  $\{e_1^{(\bar{p}\bar{o}_i)}, e_2^{(\bar{p}\bar{o}_i)}, \dots, e_{N_i}^{(\bar{p}\bar{o}_i)}\}$  with the origins  $O^{(\bar{p}\bar{o}_i)}$  that locally capture the data points  $\{\xi^{(\bar{p}\bar{o}_i)}(0), \xi^{(\bar{p}\bar{o}_i)}(t_s), \dots, \xi^{(\bar{p}\bar{o}_i)}((N_i - 1)t_s)\}$  of  $\bar{p}\bar{o}_i$ . This can be achieved by a standard method such as the principal component analysis (PCA).<sup>31</sup> Note that with a fixed sampling time, each periodic orbit  $\bar{p}\bar{o}_i$  will have different number of samples  $N_i$ . Finally, we generate a catalog of persistence diagrams  $\text{PD}^{(\bar{p}\bar{o}_1)}, \text{PD}^{(\bar{p}\bar{o}_2)}, \dots, \text{PD}^{(\bar{p}\bar{o}_M)}$  from the local projections of the periodic orbit samples sets onto their respective bases.

### III.4. Local persistence of chaotic trajectory segments

Consider the data set

$$\Xi^{(i)}(t) = \{\tilde{\xi}(t), \tilde{\xi}(t+t_s), \tilde{\xi}(t+2t_s), \dots, \tilde{\xi}(t+(N_i-1)t_s)\}, \quad (15)$$

with  $N_i$  elements that are sampled from a chaotic trajectory starting at time  $t$  and projected onto the local bases of the  $i^{\text{th}}$  periodic orbit. Let  $\text{PD}^{(i)}(t)$  be the persistence diagram obtained from this data set. We define the shadowing distance of a chaotic trajectory segment

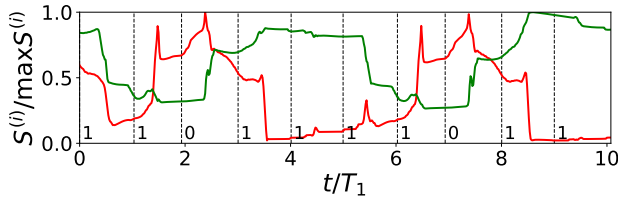


FIG. 5. Time series of the shadowing distance (16) between windows on the Rössler attractor and the  $\bar{1}$  (red) and  $\bar{01}$  (green) periodic orbits. The time axis is in units of the period of the  $\bar{1}$  orbit. Symbol sequences are read-off from the Poincaré section.

to the periodic orbit  $\bar{p}0_i$  at time  $t$  as the weighted sum

$$S^{(i)}(t) = w_0 W_p(\text{PD}_0^{(i)}(t), \text{PD}_0^{(\bar{p}0_i)}) + w_1 W_p(\text{PD}_1^{(i)}(t), \text{PD}_1^{(\bar{p}0_i)}), \quad (16)$$

The adjustable weights  $w_0$  and  $w_1$  in (16) control the respective contributions of the components and the holes to the shadowing distance. In our applications in section IV, we found the unit weights  $w_0 = w_1 = 1$  to be sufficiently informative. In order to identify a chaotic trajectory’s transient visits to the neighborhoods of the periodic orbits, we are going to measure its shadowing distance from the base-set of periodic orbits. The set of shadowing distances is the final output of state space persistence analysis. As we shall see in our applications, this measurement will allow us to predict the itinerary of a chaotic trajectory.

## IV. NUMERICAL DEMONSTRATIONS

In this section, we present two applications of state space persistence analysis. We begin with a “controlled” numerical experiment on the Rössler system.

### IV.1. Rössler system

In Fig. 2 (a) we have shown the second-order Markov partitioning of the Rössler system’s Poincaré section. Notice that the symbol sequence 00 corresponds to a narrow region. In our application, we neglect this region and take  $\{\bar{1}, \bar{01}\}$ , which we have plotted in Fig. 2 (b), as our base set. Since the Rössler system is three-dimensional and has no symmetries, we do not need a lower dimensional representation or symmetry reduction, thus we can compute the persistence of these periodic orbits in the original state space of the system.

Fig. 5 shows the shadowing distances of a chaotic trajectory of the Rössler system from the periodic orbits  $\bar{1}$  (red) and  $\bar{01}$  (green). We sampled the trajectories and the periodic orbits with a constant sampling time of  $t_s = 0.5$ , computed the Wasserstein distance (14) with  $p = q = 2$ , and for the shadowing distances used unit

weights  $w_0 = w_1 = 1$ . The symbols are read-off from the Poincaré section. It is clear from Fig. 5 that the distance of the chaotic trajectory to the periodic orbit  $\bar{1}$  has a dip when the chaotic trajectory’s itinerary has a 1. Similarly, the distance to the periodic orbit  $\bar{01}$  has a dip when the trajectory has a symbol sequence 01 or 10. These drops in the shadowing distance can be easily detected using a threshold and thus state space persistence analysis can indeed be used for inferring symbolic dynamics.

### IV.2. Kuramoto-Sivashinsky system

The Kuramoto-Sivashinsky equation was originally proposed to model the phase dynamics of reaction-diffusion systems<sup>32</sup> and instabilities of flame fronts.<sup>33</sup> Owing to its computational simplicity, nowadays the Kuramoto-Sivashinsky system is frequently chosen as the testing ground for methods to study high-dimensional chaos and turbulence.<sup>27,28,34–37</sup> In (1+1)-dimensions, the Kuramoto-Sivashinsky equation reads

$$u_t = -u u_x - u_{xx} - u_{xxx}, \quad (17)$$

where  $x \in [-L/2, L/2]$  and  $t \in [0, \infty)$  denote the space and time coordinates respectively and the subscripts imply partial derivatives. We interpret the scalar field  $u(x, t)$  as the flame front velocity and assume periodic boundary conditions, i.e.  $u(x, t) = u(x + L, t)$ . The domain length  $L$  is the sole control parameter of the Kuramoto-Sivashinsky system, whose dynamics become chaotic when  $L$  is large enough<sup>27,28</sup>.

The Kuramoto-Sivashinsky equation (17) is equivariant under continuous translations

$$g_x(\delta x)u(x, t) = u(x - \delta x, t), \quad (18)$$

where  $\delta x \in [0, L]$ , and the reflection

$$\sigma u(x, t) = -u(-x, t). \quad (19)$$

As a consequence of the symmetries (18) and (19), the Kuramoto-Sivashinsky system has relative periodic orbits, which satisfy

$$u_p = g f_{KS}^{T_p}(u_p), \quad (20)$$

where  $g \in \{g_x(\delta x_p), \sigma\}$ ,  $\delta x_p \in [0, L]$ , and  $f_{KS}^t(u)$  is the flow map induced by the time evolution under (17). As we argued in section III.1, before the persistence analysis, we must obtain a symmetry-reduced representation for the Kuramoto-Sivashinsky system. This problem was addressed in Ref. 27, which combined the first Fourier mode slice method of Ref. 20 with an invariant-polynomial method to obtain a fully symmetry-reduced representation of the Kuramoto-Sivashinsky state space. Here, we follow a slightly different approach that does not introduce any new technique, therefore, we leave the details of this to appendix A and assume that we have

a symmetry-reducing transformation  $\hat{\xi} = \mathcal{R}(u)$  for all  $u(x, t)$  of interest, such that

$$\hat{\xi} = \mathcal{R}(u) = \mathcal{R}(gu), \quad (21)$$

where  $g \in \{g_x(\delta x), \sigma\}$  and  $\delta x \in (0, L]$ . Once we obtain the symmetry-reducing transformation (21), the symmetry-reduced flow is obtained straightforwardly as

$$\hat{\xi}(t) = \hat{f}^t(\hat{\xi}(0)) = \mathcal{R}(f_{KS}^t(\mathcal{R}^{-1}(\hat{\xi}(0))))). \quad (22)$$

Note that the inverse transformation  $u = \mathcal{R}^{-1}(\hat{\xi})$  cannot be unique, since the symmetry reduction (21) maps all symmetry-equivalent states to one. However, this nonuniqueness makes no difference on the symmetry-reduced flow (22), thus, any one of the available symmetry-equivalent inverses can be taken.

After the symmetry reduction (21), by definition, the relative periodic orbits (20) become periodic orbits (5). By numerically following the unstable manifolds of relative periodic orbits, Ref. 27 presented evidence that the chaotic dynamics of the Kuramoto-Sivashinsky system at  $L = 21.7$  take place in the vicinity of four relative periodic solutions all of which are unstable. We visualized these orbits along with a long chaotic trajectory in Fig. 6 as a PCA-projection where the projection bases were obtained as the first three principal components corresponding to a long ( $t \in [0, 10^5]$ ) chaotic trajectory. Four periodic orbits

$$\overline{p\bar{o}} = \{\overline{p\bar{o}}_1, \overline{p\bar{o}}_2, \overline{p\bar{o}}_3, \overline{p\bar{o}}_4\}, \quad (23)$$

with periods  $T_1 = 10.11$ ,  $T_2 = 32.37$ ,  $T_3 = 36.70$ ,  $T_4 = 36.08$ , which we plotted as red, green, blue, and magenta loops in Fig. 6, are going to form the base set for the state space persistence analysis of the Kuramoto-Sivashinsky system.

We sampled each orbit in our base set (23) with the constant sampling time  $t_s = 0.5$  and used these samples to generate local PCA-bases and persistence diagrams for each periodic orbit as described in section III.3. In Fig. 7 (a), we show the shadowing distances (16) of a long chaotic trajectory from the four periodic orbits of the Kuramoto-Sivashinsky system as a function of time, normalized by their respective maxima. In computing these distances, we used unit weights  $w_0 = w_1 = 1$  in (16) and a Wasserstein distance (14) with  $p = q = 2$ .

When the shadowing distance (16) to a particular periodic orbit is low, we expect to find the chaotic trajectory segment to have a shape similar to that of the respective periodic orbit. We illustrate that this is indeed the case on the local projections of Fig. 7 (b-e), where we show chaotic trajectory segments of different durations with initial conditions corresponding to the local minima of the shadowing distances in Fig. 7 (a) along with the projections of the periodic orbits. As further evidence, we have shown the space-time visualizations of the shadowing trajectory segments next to the periodic orbits in Fig. 7 (f-i), where the amplitude of the scalar field  $u(x, t)$

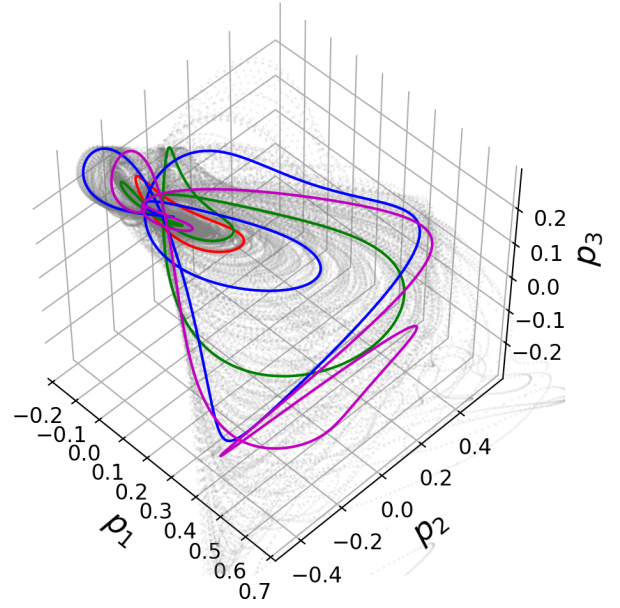


FIG. 6. A chaotic trajectory (gray dots) and four periodic orbits (red, green, blue, magenta) of the Kuramoto-Sivashinsky system projected onto three leading PCA directions obtained from a long chaotic data set.

is color-coded. Time interval shown in Fig. 7 (f) spans approximately five periods of  $\overline{p\bar{o}}_1$ , whereas for the rest of the periodic orbits one period is shown in Fig. 7 (g-i). Note that since the space-time visualizations are not symmetry reduced, the relative periodic orbits arrive at a symmetry-transformed state after one period. This can easily be seen on Fig. 7 (i), where the final state is the initial state, shifted in space by  $\delta x \approx 12.07$ . In Fig. 7 (f-h), the initial and final states are related by reflection.

## V. DISCUSSION

We presented the results of state space persistence analysis in the Rössler and the Kuramoto-Sivashinsky systems where in both cases, we see that the shadowing distance successfully captured the geometric similarities between periodic orbits and chaotic trajectory segments. The same goal in the Rössler system could have been achieved by means of a Poincaré map, however, such a tool was not available in the Kuramoto-Sivashinsky system. Thus, the success of state space persistence analysis in the Kuramoto-Sivashinsky system reveals the true potential of the method for the study of high-dimensional systems.

It is important to note that in Fig. 7 (a) at almost all times, at least one of the shadowing distances is less than 0.5, with a local minimum. This demonstrates that the spatiotemporally chaotic Kuramoto-Sivashinsky dynamics can be approximated by a Markov chain based on the four periodic solutions. Notice also that some of the step-like minima of the shadowing distances in Fig. 7 (a)

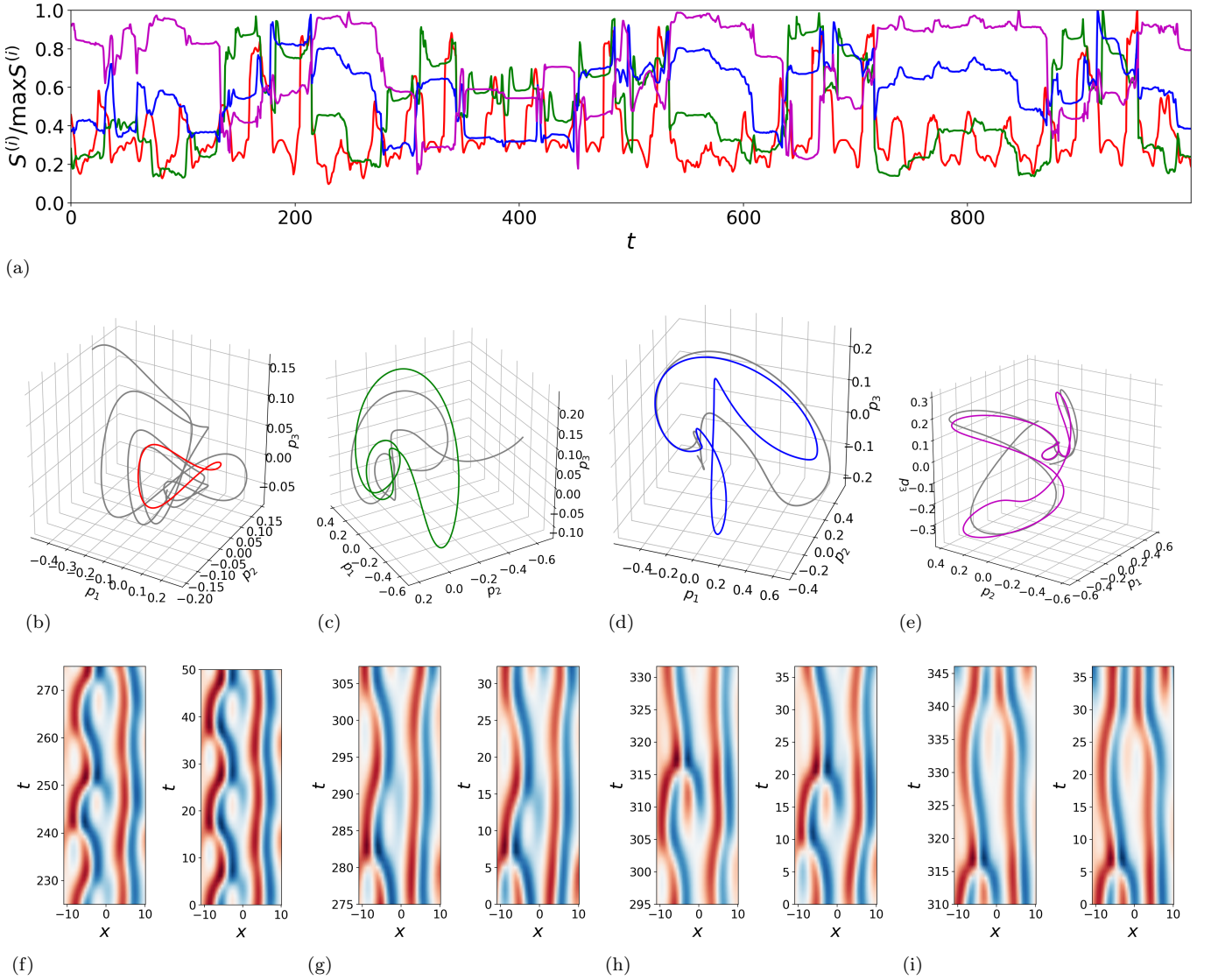


FIG. 7. (a) Shadowing distances of a long chaotic trajectory to the periodic orbits of the Kuramoto-Sivashinsky system. (b-e) Examples of shadowing trajectory segments which cover the time interval  $t \in (225, 345)$  in (a), visualized as local projections of chaotic trajectories segments (gray) onto the local PCA bases of the respective periodic orbits (colors) that are being shadowed. (f-i) Space-time visualizations of the shadowing trajectory segments (left) next to the numerically exact, periodic solutions (right) that they shadow. Time intervals of the shadowing trajectory segments (f-i) in space-time visualizations are the same intervals shown in the local projections (b-e).

coincide: For example, both red and green curves start at a low value with similar instances in the future. This reflects the partial topological similarities of  $\bar{p}\bar{o}_1$  and  $\bar{p}\bar{o}_2$ , the latter of which is in fact born on the unstable manifold of the former as demonstrated in Ref. 27. Another important observation to make on Fig. 7 (a) is that all dips in the pink time series are preceded by those of the blue curve. This suggests that  $\bar{p}\bar{o}_3$  admits a symmetry-breaking instability since  $\bar{p}\bar{o}_4$  has a non-zero spatial drift, see Fig. 7 (i). A detailed investigation and periodic-orbit-based modeling of the Kuramoto-Sivashinsky dynamics will be a subject of a future study.

## VI. CONCLUSION AND PERSPECTIVES

In this paper, we introduced state space persistence analysis for inferring the symbolic dynamics of a chaotic time series by quantifying its transient geometric similarities to the periodic solutions of the system. Our starting motivation was to have a tool for understanding high-dimensional chaos in terms of the periodic solutions of a system and we demonstrated that the state space persistence analysis can be utilized for this purpose by successfully applying it to the spatiotemporally chaotic Kuramoto-Sivashinsky system. We are now in position to apply our method to problems that are computationally

ally much more challenging, such as the simulations of the Navier-Stokes equations in three dimensions.

We would like to mention that our use of persistence is similar in spirit to the ‘‘Sliding Windows and 1-dimensional Persistence Scoring’’ (*SW1PerS*) method,<sup>38</sup> in which one constructs delay embeddings of time-series data before carrying the persistence computation in order to detect periodicities in the data. In our case, we do not need a delay embedding since we assume that we have access to the complete state space information and instead of trying to detect any periodicities in the signal, we try to identify similarities to a certain precomputed set of periodic solutions in the state space persistence analysis. One can imagine applications in which the two methods are mixed. For example, if one is searching for shadowing in a laboratory experiment in which the complete state measurement is not available, state space persistence analysis could be carried out on a delay embedding. Another interesting hybrid application could be searching for periodic solutions using the state space persistence of time-series data.

In this paper, we opted for the simplicity of presentation rather than fine-tuning our tools. As a consequence, there are a lot of aspects of state space persistence analysis that could potentially be optimized for a specific problem. For example, it could be possible to obtain cleaner shadowing signals by using different metrics between persistence diagrams or having different time-sampling schemes. Various ways by which state space persistence analysis can be optimized will be topics of our future research.

## ACKNOWLEDGMENTS

We are grateful to Predrag Cvitanović for his comments on an early version of this manuscript.

## Appendix A: State space of the Kuramoto-Sivashinsky system

We begin our numerical formulation by plugging the Fourier expansion  $u = \sum_k \tilde{u}_k(t) e^{iq_k x}$ , where  $q_k = 2\pi k/L$  and  $k = \dots, -2, -1, 0, 1, 2, \dots$ , into the Kuramoto-Sivashinsky equation (17) in order to obtain the infinite set of ODEs

$$\dot{\tilde{u}}_k = (q_k^2 - q_k^A) \tilde{u}_k - i \frac{q_k}{2} \sum_{m=-\infty}^{+\infty} \tilde{u}_m \tilde{u}_{k-m}. \quad (\text{A1})$$

Noting that the 0<sup>th</sup> Fourier mode  $\tilde{u}_0$  is decoupled from the rest and  $\tilde{u}_{-k} = \tilde{u}_k^*$  due to the realness of  $u(x, t)$ , a truncated state vector of the Kuramoto-Sivashinsky system can be expressed as

$$\xi = (a_1, b_1, a_2, b_2, \dots, a_N, b_N), \quad (\text{A2})$$

where  $(a_k, b_k) = (\text{Re } \tilde{u}_k, \text{Im } \tilde{u}_k)$  and  $N$  is the highest Fourier mode that is kept in the expansion. In our computations we used  $N = 15$ , the adequacy of which was

demonstrated in Ref. 28. In our codes, the nonlinear term in (A1) is computed pseudospectrally<sup>39</sup> and the time-stepping is carried out using the general-purpose integrator `odeint` from `scipy`,<sup>40</sup> which itself is a wrapper of `lsoda` from the `ODEPACK` library.<sup>41</sup>

It is straightforward to confirm that the action of the symmetries (18) and (19) on the real-valued state space coordinates (A2) are

$$g_x(\delta x)(a_k, b_k) = R(-k\phi)(a_k, b_k) \quad (\text{A3})$$

and

$$\sigma(a_k, b_k) = (-a_k, b_k), \quad (\text{A4})$$

where  $\phi = 2\pi \delta x/L$  and  $R(\theta)$  is the  $2 \times 2$  rotation matrix

$$R(\theta) = \begin{pmatrix} \cos \theta & -\sin \theta \\ \sin \theta & \cos \theta \end{pmatrix}. \quad (\text{A5})$$

The first Fourier mode slice method of Ref. 20 fixes the polar angle on the subspace spanned by the first Fourier mode, i.e.  $(a_1, b_1)$ , in order to eliminate the spatial drifts. It was already demonstrated in Ref. 20 that such a transformation in the Kuramoto-Sivashinsky system leads to rapid fluctuations in time, which, in general, could be regularized by rescaling the time variable. Here, we tackle this problem by a different approach, which we found simpler to use in the state space persistence analysis. Let  $\xi$  be a generic state of the Kuramoto-Sivashinsky system with nonzero components in the second Fourier mode subspace, i.e.  $a_2^2 + b_2^2 > 0$ . We search for a shifted state

$$\gamma = g_x(-\delta \hat{x})\xi \quad (\text{A6})$$

such that  $\gamma = (\hat{a}'_1, \hat{b}'_1, \hat{a}'_2, \hat{b}'_2, \dots)$  has

$$\hat{a}'_2 = 0, \hat{b}'_2 > 0. \quad (\text{A7})$$

Transforming to  $\gamma$  (A6) eliminates the continuous translation degree of freedom by fixing the phase of the second Fourier mode. However, it does not fully reduce this symmetry since if  $\gamma$  (A6) satisfies (A7) so does

$$g_x(L/2)\gamma = (-\hat{a}'_1, -\hat{b}'_1, 0, \hat{b}'_2, -\hat{a}'_3, -\hat{b}'_3, \hat{a}'_4, \hat{b}'_4, \dots). \quad (\text{A8})$$

In other words, transformation to (A6) turns the continuous translation symmetry into a discrete one. As we shall see, this discrete symmetry can be reduced by the construction of invariant polynomials similar to those introduced in Ref. 27.

After the transformation (A6), the state space has two discrete symmetries, whose actions flip the signs of a subset of the state space coordinates. Notice that the action of the reflection  $\sigma$  (A4) does not break the condition (A7) since  $\hat{\xi}'$  has  $a'_2 = 0$  and  $b_2$  is invariant under  $\sigma$ . Following the recipe of Ref. 27, we can define a reflection-reduced state vector as

$$\rho = (a_1'^2 - a_3'^2, b_1', b_2', a_1' a_3', b_3', a_3' a_4', b_4', a_4' a_5', b_5', a_5' a_6', b_6', a_6' a_7', b_7', a_7' a_8', b_8', \dots), \quad (\text{A9})$$

where we omitted  $a'_2$ , since it is set to 0. Note that (A9) is invariant under the sign change of all  $a_k$  and not invariant under the sign change of any other subset of  $a_k$ 's.

We can now turn our attention to the discrete symmetry due to the half-domain shift (A8). We should first find the representation of this symmetry on the reflection-invariant polynomial coordinates (A9). Denoting the  $k^{\text{th}}$  elements of (A9) by  $\rho_k$  it follows from inspection that

$$g_x(L/2)\rho = (\rho_1, -\rho_2, \rho_3, \rho_4, -\rho_5, -\rho_6, \rho_7, -\rho_8, -\rho_9, \\ -\rho_{10}, \rho_{11}, -\rho_{12}, -\rho_{13}, -\rho_{14}, \rho_{15} \dots). \quad (\text{A10})$$

Beginning with  $\rho_8$ , every element of  $\rho$  except  $\{\rho_{11}, \rho_{15}, \rho_{19}, \rho_{23}, \rho_{27}, \dots\}$  (every fourth element) changes its sign under the action of  $g_x(L/2)$ . Thus, we can write the final invariant polynomial coordinates as

$$\hat{\xi} = (\rho_1, \rho_2^2 - \rho_5^2, \rho_3, \rho_4, \rho_2\rho_5, \rho_5\rho_6, \rho_7, \rho_6\rho_8, \rho_8\rho_9, \rho_9\rho_{10}, \\ \rho_{11}, \rho_{10}\rho_{12}, \rho_{12}\rho_{13}, \rho_{13}\rho_{14}, \rho_{15}, \dots) \quad (\text{A11})$$

While it might appear complicated, the invariant polynomial coordinates (A9) and (A11) follow a regular pattern, and thus, are straightforward to implement. We used the symmetry-invariant state space coordinates (A11) to obtain the results of section IV.2.

- <sup>1</sup>K. T. Alligood, T. D. Sauer, and J. A. Yorke. *Chaos: An Introduction to Dynamical Systems*. Springer Berlin Heidelberg, Berlin, Heidelberg, 1997.
- <sup>2</sup>P. Cvitanović, R. Artuso, R. Mainieri, G. Tanner, and G. Vattay. *Chaos: Classical and Quantum*. Niels Bohr Inst., Copenhagen, 2019. [ChaosBook.org](http://ChaosBook.org).
- <sup>3</sup>S. Smale. Differentiable dynamical systems. *Bull. Amer. Math. Soc.*, 73:747–817, 1967.
- <sup>4</sup>P. Cvitanović. Recurrent flows: the clockwork behind turbulence. *J. Fluid Mech. Focus Fluids*, 726:1–4, 2013.
- <sup>5</sup>E. M. Cherry, F. H. Fenton, T. Krogh-Madsen, S. Luther, and U. Parlitz. Introduction to focus issue: Complex cardiac dynamics. *Chaos*, 27(9):093701, 2017.
- <sup>6</sup>M. Doebeli and I. Ispolatov. Chaos and unpredictability in evolution. *Evolution*, 68(5):1365–1373, 2014. [arXiv:1309.6261](https://arxiv.org/abs/1309.6261).
- <sup>7</sup>T. Kreilos and B. Eckhardt. Periodic orbits near onset of chaos in plane Couette flow. *Chaos*, 22:047505, 2012. [arXiv:1205.0347](https://arxiv.org/abs/1205.0347).
- <sup>8</sup>D. Lucas and R. R. Kerswell. Recurrent flow analysis in spatiotemporally chaotic 2-dimensional Kolmogorov flow. *Phys. Fluids*, 27:518–554, 2015. [arXiv:1406.1820](https://arxiv.org/abs/1406.1820).
- <sup>9</sup>P. Cvitanović and J. F. Gibson. Geometry of turbulence in wall-bounded shear flows: Periodic orbits. *Phys. Scr.*, T142:014007, 2010.
- <sup>10</sup>N. B. Budanur, K. Y. Short, M. Farazmand, A. P. Willis, and P. Cvitanović. Relative periodic orbits form the backbone of turbulent pipe flow. *J. Fluid Mech.*, 833:274–301, 2017. [arXiv:1705.03720](https://arxiv.org/abs/1705.03720).
- <sup>11</sup>D. Viswanath. Recurrent motions within plane Couette turbulence. *J. Fluid Mech.*, 580:339–358, 2007. [arXiv:physics/0604062](https://arxiv.org/abs/physics/0604062).
- <sup>12</sup>H. Edelsbrunner and J. Harer. *Persistent homology—a survey*, pages 257–282. Am. Math. Soc., Providence, 2008.
- <sup>13</sup>H. Edelsbrunner and J. Harer. *Computational topology: an introduction*. American Mathematical Soc., 2010.
- <sup>14</sup>N. Otter, M. A. Porter, U. Tillmann, P. Grindrod, and H. A. Harrington. A roadmap for the computation of persistent homology. *EPJ Data Sci.*, 6(1):17, 2017. [arXiv:1506.08903](https://arxiv.org/abs/1506.08903).
- <sup>15</sup>D. Cohen-Steiner, H. Edelsbrunner, and J. Harer. Stability of persistence diagrams. *Discrete Comput. Geom.*, 37(1):103–120, 2007.
- <sup>16</sup>U. Bauer. Ripsers, 2016. <https://github.com/Ripsers/ripsers>.
- <sup>17</sup>M. Kerber, D. Morozov, and A. Nigmatov. Hera, 2016. [https://bitbucket.org/grey\\_narn/hera](https://bitbucket.org/grey_narn/hera).
- <sup>18</sup>M. Kerber, D. Morozov, and A. Nigmatov. Geometry helps to compare persistence diagrams. In *Proceedings of the Eighteenth Workshop on Algorithm Engineering and Experiments (ALENEX)*, pages 103–112, 2016. [arXiv:1606.03357](https://arxiv.org/abs/1606.03357).
- <sup>19</sup>P. Chossat and R. Lauterbach. *Methods in Equivariant Bifurcations and Dynamical Systems*. World Scientific, Singapore, 2000.
- <sup>20</sup>N. B. Budanur, P. Cvitanović, R. L. Davidchack, and E. Siminos. Reduction of the SO(2) symmetry for spatially extended dynamical systems. *Phys. Rev. Lett.*, 114:084102, 2015. [arXiv:1405.1096](https://arxiv.org/abs/1405.1096).
- <sup>21</sup>M. Farazmand. An adjoint-based approach for finding invariant solutions of Navier-Stokes equations. *J. Fluid Mech.*, 795:278–312, 2016. [arXiv:1508.06363](https://arxiv.org/abs/1508.06363).
- <sup>22</sup>N. B. Budanur and B. Hof. Heteroclinic path to spatially localized chaos in pipe flow. *J. Fluid Mech.*, 827, R1, 2017. [arXiv:1703.10484](https://arxiv.org/abs/1703.10484).
- <sup>23</sup>N. B. Budanur and B. Hof. Complexity of the laminar-turbulent boundary in pipe flow. *Phys. Rev. Fluids*, 3:054401, 2018. [arXiv:1802.01918](https://arxiv.org/abs/1802.01918).
- <sup>24</sup>S. Mowlavi and T. Sapsis. Model order reduction for stochastic dynamical systems with continuous symmetries. *SIAM J. Sci. Comput.*, 40(3):A1669–A1695, 2018. [arXiv:1704.06352](https://arxiv.org/abs/1704.06352).
- <sup>25</sup>N. B. Budanur and M. Fleury. State space geometry of the chaotic pilot-wave hydrodynamics. *Chaos*, 29(1):013122, 2019. [arXiv:1812.09011](https://arxiv.org/abs/1812.09011).
- <sup>26</sup>N. B. Budanur, D. Borrero-Echeverry, and P. Cvitanović. Periodic orbit analysis of a system with continuous symmetry - a tutorial. *Chaos*, 25:073112, 2015. [arXiv:1411.3303](https://arxiv.org/abs/1411.3303).
- <sup>27</sup>N. B. Budanur and P. Cvitanović. Unstable manifolds of relative periodic orbits in the symmetry-reduced state space of the Kuramoto-Sivashinsky system. *J. Stat. Phys.*, 167(3):636–655, 2017. [arXiv:1509.08133](https://arxiv.org/abs/1509.08133).
- <sup>28</sup>P. Cvitanović, R. L. Davidchack, and E. Siminos. On the state space geometry of the Kuramoto-Sivashinsky flow in a periodic domain. *SIAM J. Appl. Dyn. Syst.*, 9:1–33, 2009. [arXiv:0709.2944](https://arxiv.org/abs/0709.2944).
- <sup>29</sup>F. Christiansen, P. Cvitanović, and V. Putkaradze. Spatiotemporal chaos in terms of unstable recurrent patterns. *Nonlinearity*, 10:55–70, 1997. [arXiv:chao-dyn/9606016](https://arxiv.org/abs/chao-dyn/9606016).
- <sup>30</sup>Y. Lan and P. Cvitanović. Unstable recurrent patterns in Kuramoto-Sivashinsky dynamics. *Phys. Rev. E*, 78:026208, 2008. [arXiv:0804.2474](https://arxiv.org/abs/0804.2474).
- <sup>31</sup>I. T. Jolliffe. *Principal Component Analysis, Second Edition*. Springer, 2002.
- <sup>32</sup>Y. Kuramoto and T. Tsuzuki. Persistent propagation of concentration waves in dissipative media far from thermal equilibrium. *Progr. Theor. Phys.*, 55:365, 1976.
- <sup>33</sup>G. I. Sivashinsky. Nonlinear analysis of hydrodynamical instability in laminar flames - I. Derivation of basic equations. *Acta Astronaut.*, 4:1177, 1977.
- <sup>34</sup>P. Holmes, J. L. Lumley, and G. Berkooz. *Turbulence, Coherent Structures, Dynamical Systems and Symmetry*. Cambridge Univ. Press, Cambridge, 1996.
- <sup>35</sup>D. Goluskin and G. Fantuzzi. Bounds on mean energy in the Kuramoto-Sivashinsky equation computed using semidefinite programming. *Nonlinearity*, 32(5):1705–1730, 2019. [arXiv:1802.08240](https://arxiv.org/abs/1802.08240).
- <sup>36</sup>J. Pathak, A. Wikner, R. Fussell, S. Chandra, B. R. Hunt, M. Girvan, and E. Ott. Hybrid forecasting of chaotic processes: Using machine learning in conjunction with a knowledge-based model. *Chaos*, 28(4):041101, 2018. [arXiv:1803.04779](https://arxiv.org/abs/1803.04779).
- <sup>37</sup>J. Pathak, Z. Lu, B. R. Hunt, M. Girvan, and E. Ott. Using machine learning to replicate chaotic attractors and calculate lyapunov exponents from data. *Chaos*, 27(12):121102, 2017. [arXiv:1710.07313](https://arxiv.org/abs/1710.07313).
- <sup>38</sup>J. A. Perea and J. Harer. Sliding windows and persistence: An application of topological methods to signal analysis. *Found. Comput. Math.*, 15(3):799–838, 2015. [arXiv:1307.6188](https://arxiv.org/abs/1307.6188).
- <sup>39</sup>C. Canuto, M. Y. Hussaini, A. Quarteroni, and T. A. Zang. *Spec-*

*tral Methods: Evolution to Complex Geometries and Applications to Fluid Dynamics.* Springer, New York, 2007.

<sup>40</sup>E. Jones, T. Oliphant, P. Peterson, et al. SciPy: Open source

scientific tools for Python, 2001.

<sup>41</sup>A. C. Hindmarsh. ODEPACK, a systematized collection of ODE solvers. In R. S. Stepleman, editor, *Scientific Computing*, volume 1, pages 55–64. North-Holland, Amsterdam, 1983.